Remote Sensing of the Thermodynamic State of the Atmospheric Boundary Layer by Ground-Based Microwave Radiometry

J. GÜLDNER AND D. SPÄNKUCH

German Weather Service, Meteorological Observatory Potsdam, Potsdam, Germany

(Manuscript received 25 May 2000, in final form 2 October 2000)

ABSTRACT

First results are presented of 18 months' experience with a microwave profiler that has been in operation in an unattended mode. Profiles of temperature and water vapor were retrieved without bias by a statistical regression method that was more accurate as opposed to a neural network approach, in particular for water vapor. Cloud liquid water was estimated by a neural network. The accuracy of the retrieved profiles estimated against quasisimultaneous radiosonde measurements are of comparable quality to that of the retrievals of ground-based Fourier transform infrared (FTIR) measurements. For temperature, the accuracy is about 0.6 K near the surface and less or equal to 1.6 K up to 7 km in summer and 4 km in winter. For water vapor, the corresponding values are 0.2–0.3 g m^{-3} near the surface and 0.8–1.0 g m^{-3} from 1- to 2-km altitude. The vertical resolution, however, is worse than that of FTIR measurements.

Two case studies—a 1-week anticyclonic situation and 1 day with a cold front passage—demonstrate the capacity of microwave radiometry to sense the thermodynamic structure of the lower troposphere up to 3–4 km quasi-continuously with reasonable accuracy and height resolution, interrupted only during precipitation events. The diurnal course of temperature and humidity as well as the weakening of the amplitudes and decay with altitude was traced up to 4 km. Considerable structure was found, too, in the liquid water profile during the passage of the cold front. The cloud base retrieved from the microwave data corresponded well with collocated ceilometer measurements.

1. Introduction

There has been increasing interest in continuous monitoring of the atmospheric boundary layer structure. There are many reasons for that, for example, short-term meteorological forecasting and air pollution control.

A fleet of ground-based remote sounding tools has been developed and successfully introduced to tackle this goal (e.g., Clifford et al. 1994; Wilczak et al. 1996). There are active and passive remote sounding devices, both with advantages and drawbacks. Active devices except sodars are in general more expensive and need more care for operation than passive devices. On the other hand, passive devices have less complicated hardware. This makes them particularly attractive for operation in an unattended mode. However, their vertical resolution is poorer than that of active sensors due to their smooth weighting function characteristics. Thus ''the combination of data from active, passive (and in situ) sensors is the most promising way to achieve success in profiling thermodynamic variables throughout the full depth of the troposphere'' (Stankov 1998; see also Westwater 1997). The combined approach of available ground-based sounding techniques was tested in several extensive field campaigns around the world (Smith et al. 1990; Stokes and Schwartz 1994; Westwater et al. 1999a). Two passive techniques have been successfully applied for temperature and humidity sensing: microwave radiometry (e.g., Troitsky et al. 1993; Westwater et al. 1999b) and Fourier transform infrared (FTIR) emission spectroscopy (e.g., Feltz et al. 1998; Smith et al. 1999). Microwave radiometers sense the atmosphere during nonprecipitating conditions (e.g., Hogg et al. 1983; Güldner and Spänkuch 1999). Their output contains additional information about the cloud liquid water content, but they have not been used for humidity profiling up to now. Radiance IR spectra contain additional information on cloud properties (e.g., Smith et al. 1993; Collard et al. 1995), aerosols (Lubin and Simpson 1994; Spänkuch et al. 1999, 2000), and trace gases like ozone (Puckrin et al. 1996; Spänkuch et al. 1998; Evans and Puckrin 1999a), carbon monoxide (Evans and Puckrin 1999b), and others. The retrieval of vertical temperature and humidity profiles is impeded at cloudy field of view, however, and is restricted to the subcloud layer.

In this paper, the application of a novel microwave

Corresponding author address: Dr. Jürgen Güldner, Deutscher Wetterdienst, Meteorologisches Observatorium Potsdam, Postfach 60 05 52, 14405 Potsdam, Germany.
E-mail: juergen.gueldner@dwd.de

TABLE 1. Specification of the TP/WVP 3001 microwave profiler.

Frequency (GHz)	Beamwidth* (°)	Dominant influencing parameters
22.235		Water vapor Cloud liquid water
23.035		
23.835	5.5	
26.235		
30.000	4.5	
51.250		Temperature Cloud liquid water
52.280	2.7	
53.850		
54.940		
56.660		
57.290		
58.800	2.3	

* Defined as full-width half-power (3 dB) beamwidth.

FIG. 1. The microwave profiler TP/WVP-3001.

technique for simultaneous profiling of temperature, humidity, and liquid water content is presented using data from the microwave profiler TP/WVP-3001 from Radiometrics Corporation. Its potential is demonstrated by statistical comparisons with radiosonde data for 3-month periods in summer and winter and by two well-documented case studies. The profiler has been in operation at the Lindenberg Meteorological Observatory (52.22°N, 14.12°E) since November 1998.

2. Radiometer description

Specific characteristics of the TP/WVP 3001 microwave profiler of Radiometrics Corporation are listed in Table 1. The 12 channels are thoroughly selected by radiative transfer calculations and subsequent eigenvalue analysis of the covariance matrix of the corresponding weighting functions. They are located between 22 and 59 GHz (Solheim et al. 1998). The 22.235-GHz frequency was preselected in the selection procedure due to the highest sensitivity to altitude for water vapor. Information on the atmospheric temperature structure is contained along the 60-GHz oxygen resonance line. The water vapor resonance line at 22.2-GHz is used for water vapor profiling. Both features are affected by cloud liquid water and are used to estimate the cloud liquid water profile, too. In addition to the retrieval channels, the instrument shown in Fig. 1 contains a passive infrared pyrometer centered around 1000 cm^{-1} for information on cloud-base temperature. Cloud-base temperature and cloud-base height are useful constraints for water vapor and liquid water retrievals as shown by Han and Westwater (1995).

The water vapor channels are calibrated by means of tipping curves (see, e.g., Decker and Schröder 1991); the temperature channels are calibrated by a liquid nitrogen cold target. The original bandwidth is 380 MHz edge-to-edge. However, in order to avoid phase noise of the synthesizer, a region of 80 MHz in the center of this bandpass was excluded. Thus the true bandpass of the channels is 300 MHz.

A full cycle of the 12 brightness temperatures is performed in about 12 min. The profiles are processed in a real-time mode enabling a quasi-continous monitoring of the thermodynamic state of the lower troposphere interrupted only during moderate and heavy precipitation.

3. Retrieval algorithm and comparison with radiosondes

There are several methods (e.g., Houghton et al. 1984) to solve the radiative transfer equation

$$\mathbf{y} = A\mathbf{x} + \varepsilon, \tag{1}$$

where $\mathbf{x}$ is the temperature or humidity profile to be retrieved, $\mathbf{y}$ is the vector of spectral measurements, ε contains the corresponding measurement errors, and A is an operator that links the profiles with the radiative parameters. Relationship (1) is nonlinear and there does not exist any unique solution. Generally, the cost function

$$V(C) = E\|\mathbf{x}_e - \mathbf{x}\| \tag{2}$$

is minimized, where $\mathbf{x}_e$ and $\mathbf{x}$ are the estimated and the true profile, respectively. The best linear unbiased solution is given by

$$\mathbf{x}_e = \mathbf{K}\mathbf{A}^{\mathrm{T}}(\mathbf{A}\mathbf{K}\mathbf{A}^{\mathrm{T}} + S)^{-1}y, \tag{3}$$

where $\mathbf{K}$ is the covariance of temperature or humidity and S is the error covariance; $\mathbf{A}^{\mathrm{T}}$ is the transpose matrix of $\mathbf{A}$.

The solution (3) needs a fast line-by-line code for rapid simulation of the spectral measurements and a profound knowledge of the relevant spectroscopic quantities. This is similar to the physical iterative solution described by Smith (1970) and Smith et al. (1999).

The application of the original neural network described in Solheim et al. (1998) uses a standard back propagation algorithm. It showed systematic retrieval errors, in particular for water vapor indicating inaccuracies in the radiative transfer calculations and/or the

calibration procedure. In order to avoid this error source Eq. (1) was solved by statistical regression

$$\mathbf{x}_e = \mathbf{C}_{xy}\mathbf{C}_{yy}^{-1}\mathbf{y}, \quad (4)$$

where $\mathbf{C}_{xy}$ is the covariance of the measurement vector $\mathbf{y}$ and simultaneous radiosonde profiles $\mathbf{x}$, and $\mathbf{C}_{yy}$ the covariance matrix of all measurements $\mathbf{y}$ of the comparisons. Thus the solution $\mathbf{x}_e$ is not affected by radiative transfer calculations but by measurements only. In order to improve the retrieval accuracy near the surface, the vector $\mathbf{y}$ contains additionally the measured ground-based values of temperature and humidity at the site. Other parameters, for example, total precipitable water taken from a global positioning system (GPS) station (Businger et al. 1996; Ware et al. 2000) can be added to $\mathbf{y}$, too, if available.

The covariances were calculated for the site from 237 cases in summer and 254 cases in winter. Cloud liquid water profiles were retrieved by the original neural network provided by Solheim et al. (1998).

The comparison between radiosonde and MWP profiles is shown in Fig. 2 for summer (June to August 1999), and in Fig. 3 for winter (November 1998–February 1999). The top curve represents temperature and the bottom curve shows vapor density. The standard deviation of the radiosondes used in the comparison is given by heavy solid lines, the results from the neural network are given by solid lines. The dashed lines give the bias of the neural network. The results of the statistical regression are given by the solid lines with squares. The climatological variance is by and large representative for the site with increasing/decreasing temperature variance with height in winter/summer and larger water vapor variance in summer than in winter. There is considerable bias in the water vapor retrievals of the neural network with, on average, moister retrievals than radiosonde measurements throughout the lower troposphere. The temperature retrievals of the neural network are on average warmer throughout the lower troposphere in winter and from about 300 m to 1.5 km in summer.

Removal of the bias in the neural network retrieval (not shown) leads to comparable results with those of the statistical regression for temperature but not for water vapor. The temperature retrievals differ by about 0.2 K for altitudes above about 0.8 km in winter and 2 km in summer with slightly better accuracy for the statistical regression method. The temperature rms error is about 0.6 K near the surface due to the incorporation of the direct near-surface values in the regression, and reaches about 1 K between 0.5 and 1.3 km in summer and at about 0.3 km in winter, respectively. The error is, however, less than or equal to about 1.6 K up to 7 km in summer and 4 km in winter.

The regression approach gives considerably better results than the neural network in case of water vapor retrieving. The improvement by the regression method is with 0.3 g m^{-3} particularly distinct in winter between

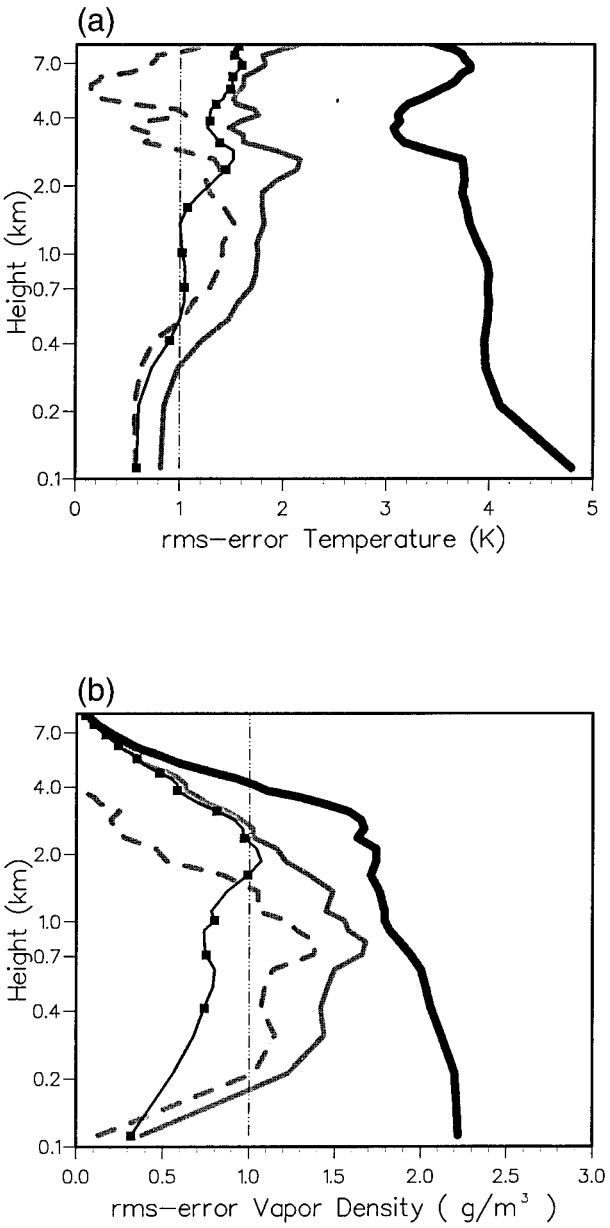

FIG. 2. Retrieval error statistics for (top) summer and (bottom) temperature vapor density based on more than 200 intercomparisons with radiosonde data. Heavy solid line—standard deviation of the radiosondes used in the intercomparison; solid line—neural network; solid line with squares—statistical regression; dashed line—bias defined as retrieval by neural network minus radiosonde.

0.7 and 2 km where the rms error reaches a broad maximum with 0.8 g m^{-3}. The error near the surface is about 0.2 g m^{-3}. In summer, the error is about 0.3 g m^{-3} near the surface and increases up to 1.0 g m^{-3} at 2 km where the improvement vanishes against the neural network retrieval without bias. Both temperature and water vapor retrieval accuracies are of comparable quality to the results of Smith et al. (1999) by means of ground-based FTIR emission spectroscopy. The bias of

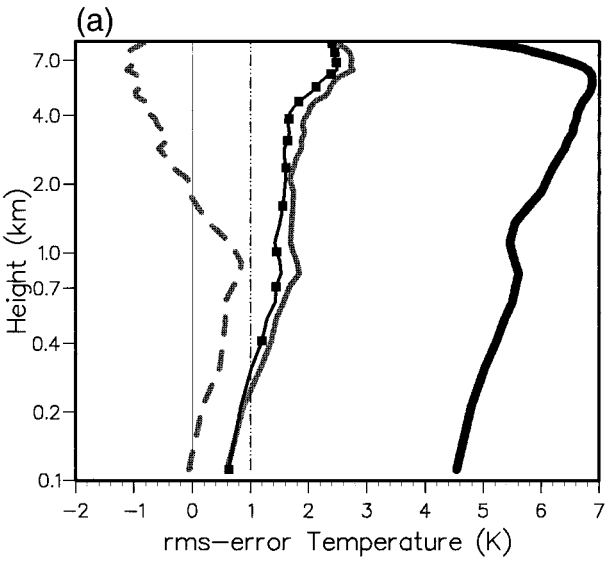

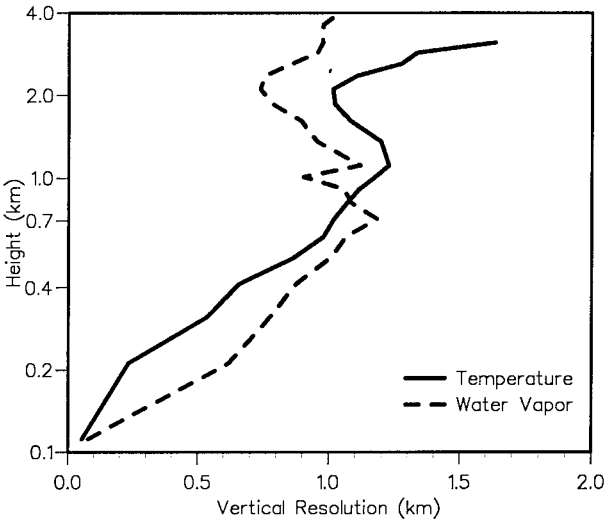

FIG. 4. Vertical resolution for temperature (solid line) and water vapor density (dashed line).

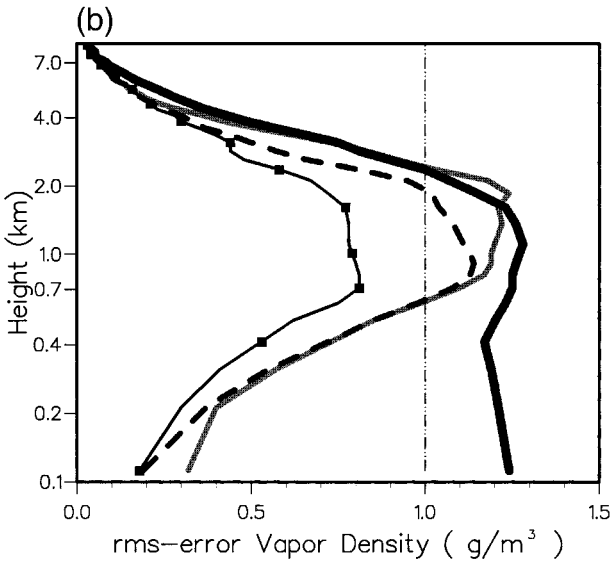

FIG. 3. The same as in Fig. 2 but for winter.

the neural network retrievals has the same sign as the FTIR results, but its amount is significantly higher.

The use of radiosonde measurements as truth reference has been debated frequently. The reference is not an ideal one due to several reasons. There are not only the inherent measurement errors of radiosondes, about 0.5 K for temperature and 10% for relative humidity (Pratt 1985; Schmidlin 1988). There is the dislocation of the ascending balloon compared to the indirect sensed atmospheric volume. Additionally, short-term variations of both parameters are quite frequent, particularly for water vapor that reaches 5%–10% in total precipitable water (e.g., Spänkuch et al. 2000). The attainable accuracy should thus be better than the estimate derived from the intercomparison. More weight has the comparison with the FTIR results of Smith et al. (1999), also for the following discussion of resolving power.

4. Vertical resolution of the retrieved profiles

The vertical resolving power is another important characteristic of a retrieval system besides the attainable retrieval accuracy. Unfortunately, an appropriate definition of vertical resolution does not exist yet. In satellite meteorology, the vertical resolution is linked with the spread of the more or less bell-shaped weighting functions (Conrath 1972; Thompson 1982). The weighting functions of ground-based passive systems decrease exponentially with altitude (see, e.g., Spänkuch et al. 1996) so that the definition of satellite meteorology cannot be applied. In order to overcome this difficulty, Smith et al. (1999) defined the vertical resolution as the half-width of the vertical interlevel covariance functions of the retrieval errors, written for the temperature as

$$C(z_0, z) \equiv \frac{\sum_{i=1}^{N} [T_r(z_0) - T(z_0)]\,[T_r(z) - T(z)]}{\sqrt{\sum_{i=1}^{N} [T_r(z_0) - T(z_0)]^2 \sum_{i=1}^{N} [T_r(z) - T(z)]^2}}, \quad (5)$$

where T_r is the retrieved temperature, T is the radiosonde temperature taken as a true value, z is altitude, and z_0 is the reference altitude for which the vertical resolution is being defined. Here N is the number of retrieval/radiosonde matches.

Figure 4 shows the vertical resolution for temperature as solid line and water vapor density as dashed line. The vertical resolution decreases continuously from

TABLE 2. Synoptic conditions at Lindenberg from 25 to 31 Jul 1999.

Day	Synoptic pattern* (''Großwetterlage'')	Air mass*	Horizontal visibility (km) at 1200 UTC
25 Jul	HB	mT_p	18
26 Jul	HB	mT_p/mP	25
27 Jul	HNFa	mP	40
28 Jul	HNFa	cT_p	40
29 Jul	HNFa	cT_p	45
30 Jul	HNFa	cT_p	35
31 Jul	HNFa	cT_p	30

HB—Central European ridge with high pressure over central Europe.

HNFa—High over the Norwegian Sea and Fennoscanida with anticyclonic flow.

* Taken from DWD (1999).

nearly 50 m near the surface to about 1.2 km at 1 km for temperature and to about 1.2 km at 700 m for water vapor. There is some improvement in the vertical resolving power above this height for water vapor down to 0.7 at 2 km. For temperature, the vertical resolution deteriorates further above 2-km altitude. The vertical resolution is about three times worse within the first km compared to the IR sounding capability (Smith et al. 1999), but of comparable magnitude aloft. The decline of vertical resolution with height shown in Fig. 4 corresponds to the results of Westwater et al. (2000). These authors evaluated the resolution by the response of the brightness temperature to a unit positive perturbation in a 1-km-thick layer at certain heights.

We note like Smith et al. (1999) that the vertical resolution defined in the way described is at the lower limit. The analysis of the following cases indicates a considerably higher vertical resolution capacity than given by the definition applied.

5. Case studies

a. The period from 25 to 31 July 1999

This case is a good example of the potential of the new technique in case of nondramatic meteorological developments. High pressure systems affected the weather in central Europe at the end of July 1999. This nonprecipitating period enabled uninterrupted microwave measurements during that time. The high pressure was the result of stable large-scale synoptic patterns, a central European ridge, called Grosswetterlage HB, on 25 and 26 July followed by a high over the Norwegian Sea and Fennoscandia, known as Grosswetterlage HNFa. Both Grosswetterlagen are characterized by above-normal temperature and below-normal precipitation (Bürger 1958; Gerstengarbe et al. 1993). Their frequencies are 4.5% and 1%, respectively. Some relevant synoptic characteristics of that period are compiled in Table 2. The change from HB to HNFa was

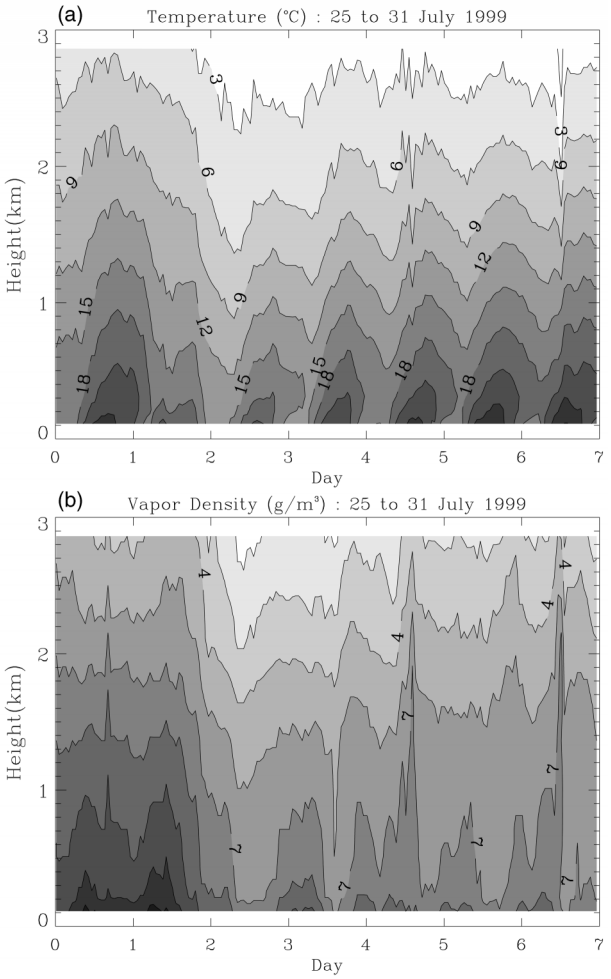

FIG. 5. Height–time section of (top) temperature and (bottom) absolute humidity from 25 to 31 Jul 1999 at Lindenberg.

accompanied by a change from temperate marine tropical air mass to polar air mass, which was replaced on 28 July till the end of the period by continental tropical air mass. Simultaneously, the visibility improved from about 20 to 40 km when the marine tropical air mass was replaced by marine polar air and lateron by continental tropical air mass with slightly decreasing visibility during its aging process.

The thermodynamic variations of the lower troposphere derived from the microwave data are shown in Fig. 5 as height–time sections of temperature (top) and absolute humidity (bottom) and in Fig. 6 as course of both parameters, (a) temperature and (b) absolute humidity, at selected altitudes. Figure 6b, top, contains, too, the total column amount of water vapor of the collocated GPS station. Well-known facts such as the diurnal cycle of both parameters, its decreasing amplitude, and phase retardation with height are clearly discernible. The diurnal temperature cycle is more regular than the moisture cycle, as expected, and can be traced up to 4 km where the amplitude is of the order of 1°–2°C. Near-

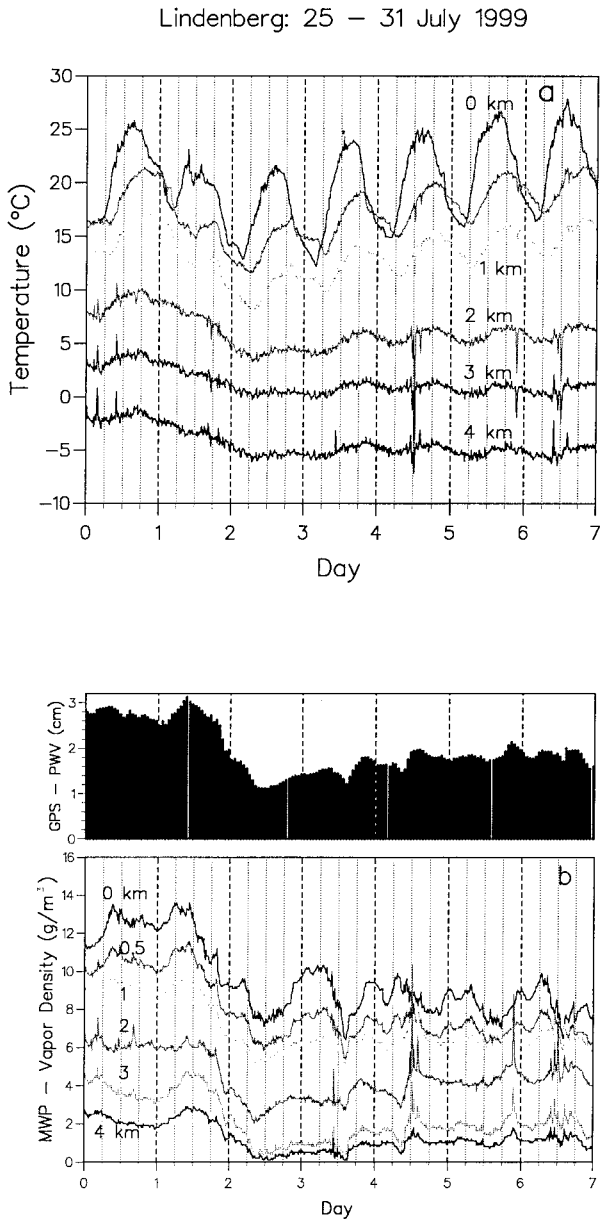

FIG. 6. (a) Temperature vs time at selected altitudes from 0 to 4 km. (b) (bottom) Vapor density vs time at selected altitudes from 0 to 4 km. (top) Total precipitable water from the collocated GPS station.

surface temperature inversions during the early morning hours, which were observed on all days except day 2 are common features of the synoptic patterns HB and HNFa. The turnover from one air mass to another (see Table 2) is particularly distinct in Fig. 6 in the sharp drop of 50% in absolute humidity in the lowest km and even more above that layer, accompanied by decreasing humidity gradient in the uppermost layer from 1200 UTC 26 July till 0800 UTC 27 July. At the same time, the temperature decreased at all altitudes, superimposed by the diurnal cycle in the lowest 2 km, to the absolute minimum during the early morning of the third day. Afterward the temperature increased again till day 7 up to the same level than before in the lowest km. The increase was somewhat less above whereas general humidity increase was observed only from 2 km onward. The increase on day 3 started at 2 km from about 2 to 3.5 g m^{-3} at about 0800 UTC, earlier than in all other levels. In the lowest 0.5 km and at the uppermost two levels the decline continued till 1200 UTC although more slowly than before. At 1 km, however, the humidity remained nearly constant till 1200 UTC.

Another interesting feature is the occasional occurrence of sharp humidity drops throughout the lower troposphere of about 2–4-h duration as on days 4 and 7 shortly after noon, and on day 5 before noon. These drops are not reflected in the temperature course. Therefore they are probably caused by horizontal advection of rather dry air parcels. Another drop within the first 6 h of day 5 is limited to the first km with simultaneous increase at 3 and 4 km and no change at 2 km. To save space we close our discussion of this case study with the moisture analysis of day 1 despite further interesting aspects. There are ups and downs in absolute humidity during that day in all levels except at 2 km. Nearly constant values around 6 g m^{-3} were observed for about 20 h, namely, from 1000 till 0600 UTC of the following day and interrupted only by some, however considerable, outbreaks. Formation and dissipation of clouds at the top of the boundary layer is not supported by observations. There were mostly low-level clouds in the morning and midlevel clouds in late evening. Similar cloud conditions were observed on the other days but with partly clear nights to the end of the period. The spikes in Fig. 6 that are often accompanied by sharp drops in temperature are most likely artifacts.

b. Passage of a cold front

A cold front passed the site in the afternoon of 18 December 1998. The course of temperature and humidity on that day is shown in Fig. 7. Liquid water content and absolute humidity are given in Fig. 8 at the time of the front passage. A ridge of high pressure from the Azores to the Baltic states determined the weather in the morning with rather high temperatures and low moisture in the descending air and only a few high and midlevel clouds. The most prominent feature is a strong temperature inversion of more than 10°C of 1-km depth, which weakened during the late morning. This process is well documented by the microwave measurements as shown by intercomparison with the radiosonde data taken every 6 h (Fig. 9).

The passage of the cold front at 1500 UTC was indicated by a sudden increase in humidity. The increase was tracable up to 4 km with maximum values of about 6 g m^{-3} between about 0.7 and 1.5 km from 1830 to 2000 UTC and the occurrence of stratocumuli at 800

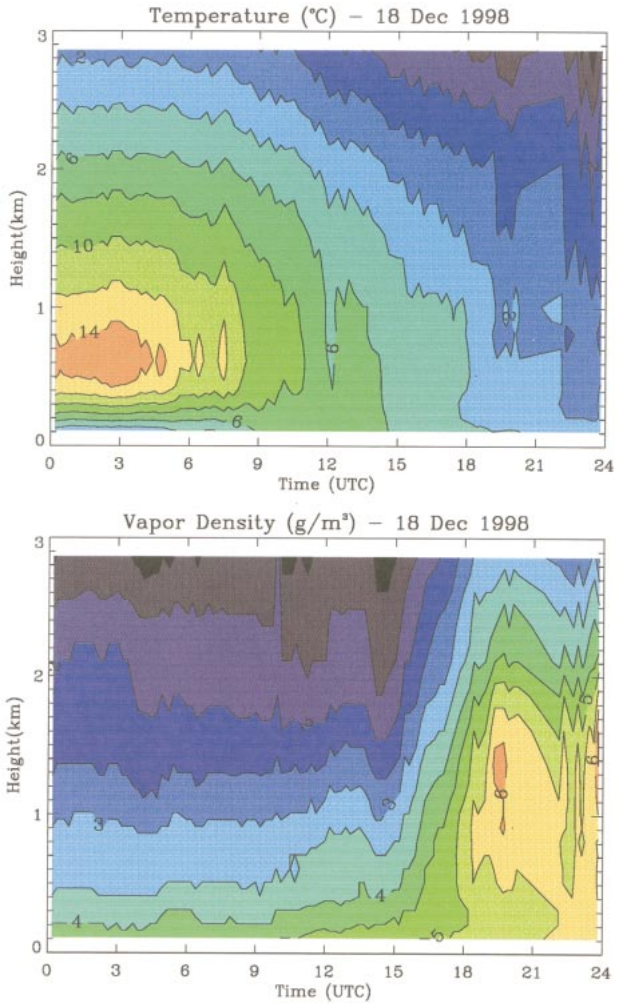

FIG. 7. Height–time section of (top) temperature and (bottom) absolute humidity on 18 Dec 1998.

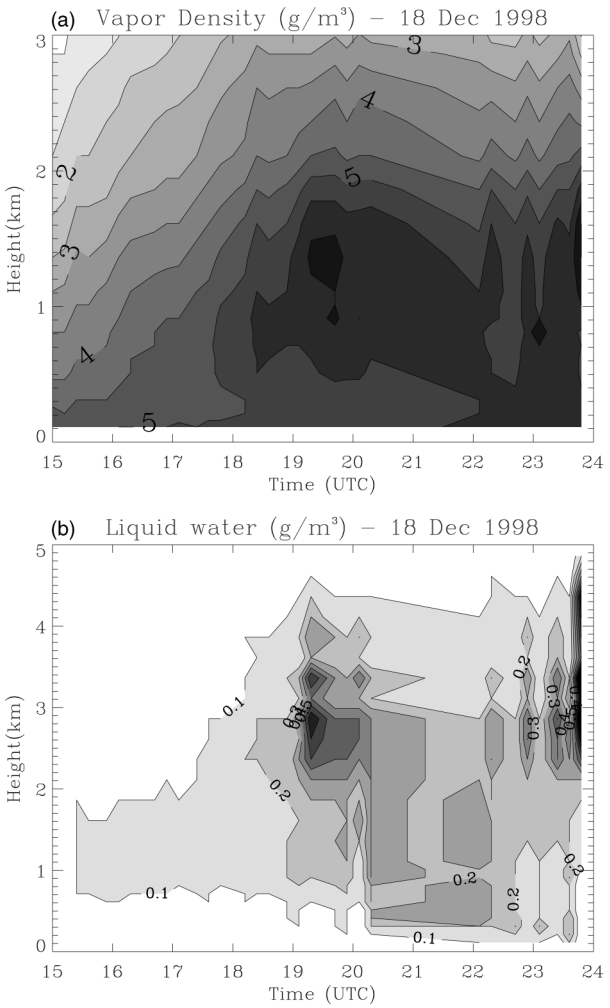

FIG. 8. Height–time section of (top) vapor density and (bottom) cloud liquid water on 18 Dec 1998 during the passage of a cold front.

m. The intercomparison with the radiosonde data shown in Fig. 9 demonstrates the good quality of the retrievals.

The liquid water content was estimated between 0.1 and less than 0.2 g m^{-3}. The geometric cloud thickness increased, according to Fig. 8, permanently but particularly heavily shortly after 1700 UTC with a rate of more than 1 km h^{-1}. The liquid water content per volume did not increase remarkably until 1900 UTC, however, when the maximum was reached with 0.7 g m^{-3} at 3-km height and up to 0.3 g m^{-3} at 4 km for a short while. Isolated raindrops were reported between 1946 and 2035 UTC, and 2110 and 2118 UTC, respectively, with light rain in between. The total rain intensity was 0.1 mm. There was, different from humidity and temperature, no possibility of validation of the retrieved cloud water content. Nevertheless, even though the absolute values are less fixed than for the other two parameters, the liquid water structure within the cloud is surely adequately reflected. Note that remote sensing systems, active or passive, operating at shorter wave-

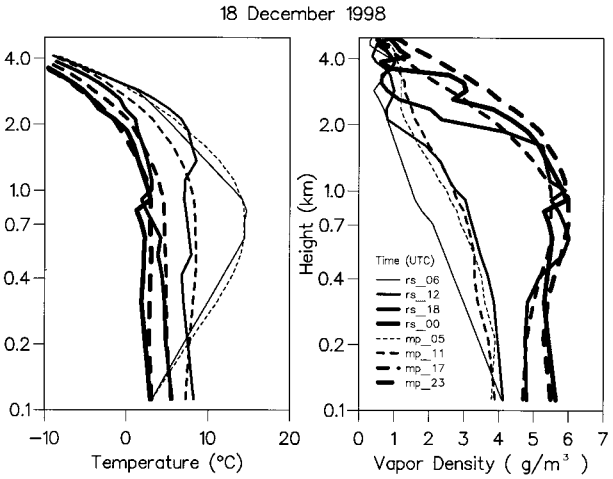

FIG. 9. Intercomparison between retrieved (dashed lines) and radiosonde profiles (solid lines): (left) temperature, (right) absolute humidity. The line width increases with time from 0600, 1200, 1800, to 2400 UTC.

lengths than in the microwave domain are not able to monitor such an event.

6. Summary and conclusions

A microwave profiler has been operating at the Meteorological Observatory Lindenberg for 18 months in an unattended mode. A regression method was developed and applied to retrieve temperature and water vapor profiles without bias. This method was superior to the neural network approach, in particular for water vapor. Liquid water was estimated by the original neural network provided by Solheim et al. (1998). The accuracy of the retrieved temperature and water vapor profiles were estimated against radiosonde profiles. The accuracy of the retrieved temperature profiles is about 0.6 K near the surface and less than or equal to 1.6 K up to 7 km in summer and 4 km in winter. The accuracy of water vapor profiles is 0.2–0.3 g m^{-3} near the surface and 0.8–1.0 g m^{-3} from 1- to 2-km altitude. These amounts are of comparable quality to those derived by Smith et al. (1999) by means of ground-based FTIR measurements. The vertical resolution is within the first kilometer about three times worse than corresponding data from FTIR measurements but of the same order aloft.

Two case studies demonstrate that microwave radiometers are powerful tools to sense the thermodynamic structure of the lower troposphere continuously by providing profiles of temperature, humidity, and cloud liquid water up to 3–4 km with reasonable accuracy and height resolution. The measurements are interrupted only during moderate to heavy rain. The diurnal course of temperature and humidity with weakening of the amplitudes and decay is traceable up to 4 km. The derived structures show that the vertical resolving power is much better than estimated from the interlevel covariances of the retrieval errors. Considerable structure was found, too, in the liquid water profile during the passage of a cold front. The cloud base corresponded well with simultaneous ceilometer data. A combination of both passive remote sensing devices, FTIR and microwave, is expected to improve the quality of the retrievals. It provides additional information on trace gases, cloud radiative properties, and hence microphysical cloud properties near the cloud base.

Acknowledgments. We thank H. Steinhagen for his support during the installation and operation of the microwave profiler at the Meteorological Observatory Lindenberg.

REFERENCES

Bürger, K., 1958: *Zur Klimatologie der Grosswetterlagen.* Vol. 45, Deutscher Wetterdienst, 79 pp.

Businger, S., and Coauthors, 1996: The promise of GPS in atmospheric monitoring. *Bull. Amer. Meteor. Soc.,* **77,** 5–18.

Clifford, S. F., J. C. Kaimal, R. J. Lataitis, and R. G. Strauch, 1994: Ground-based remote profiling in atmospheric studies: An overview. *Proc. IEEE,* **82,** 313–355.

Collard, A. D., S. A. Ackerman, W. L. Smith, X. Ma, H. E. Revercomb, R. O. Knuteson, and S.-C. Lee, 1995: Cirrus cloud properties derived from high spectral resolution infrared spectrometry during FIRE II. Part III: Ground-based HIS results. *J. Atmos. Sci.,* **52,** 4264–4275.

Conrath, B. J., 1972: Vertical resolution of temperature profiles obtained from remote sensing measurements. *J. Atmos. Sci.,* **29,** 1262–1272.

Decker, M. T., and J. A. Schroeder, 1991: Calibration of ground-based microwave radiometers for atmospheric remote sensing. NOAA Tech. Memo. ERL WPL-197, 16 pp.

DWD, 1999: *Die Grosswetterlagen Europas.* Vol. 52. Deutscher Wetterdienst, 8 pp.

Evans, W. F. J., and E. Puckrin, 1999a: Remote sensing measurements of tropospheric ozone by ground-based thermal emission spectroscopy. *J. Atmos. Sci.,* **56,** 311–318.

——, and ——, 1999b: Combined measurements of thermal emission and solar absorption of atmospheric carbon monoxide. *Atmos. Environ.,* **33,** 2081–2088.

Feltz, W. F., W. L. Smith, R. O. Knuteson, H. E. Revercomb, H. M. Woolf, and H. B. Howell, 1998: Meteorological applications of temperature and water vapor retrievals from the ground-based Atmospheric Emitted Radiance Interferometer (AERI). *J. Appl. Meteor.,* **37,** 857–875.

Gerstengarbe, F.-W., P. C. Werner, W. Busold, U. Rüge, and K.-O. Wegener, 1993: *Katalog der Grosswetterlagen Europas nach Paul Hess und Helmuth Brezowsky 1881–1992.* Vol. 113, Deutscher Wetterdienst, 249 pp.

Güldner, J., and D. Spänkuch, 1999: Results of year-round remotely sensed integrated water vapor by ground-based microwave radiometry. *J. Appl. Meteor.,* **38,** 981–988.

Han, Y., and E. R. Westwater, 1995: Remote sensing of tropospheric water vapor and cloud liquid water by integrated ground-based sensors. *J. Atmos. Oceanic Technol.,* **12,** 1050–1059.

Hogg, D. C., F. O. Guiraud, J. B. Snider, M. T. Decker, and E. R. Westwater, 1983: A steerable dual-channel microwave radiometer for measurement of water vapor and liquid in the troposphere. *J. Climate Appl. Meteor.,* **22,** 789–806.

Houghton, J. T., T. W. Taylor, and C. D. Rodgers, 1984: *Remote Sounding of Atmospheres.* Cambridge University Press, 343 pp.

Lubin, D., and A. S. Simpson, 1994: The longwave emission signature of urban pollution: Radiometric FTIR measurement. *Geophys. Res. Lett.,* **21,** 37–40.

Pratt, R. W., 1985: Review of radiosonde humidity and temperature errors. *J. Atmos. Oceanic Technol.,* **2,** 404–407.

Puckrin, E., W. F. J. Evans, and T. A. B. Adamson, 1996: Measurement of tropospheric ozone by thermal emission spectroscopy. *Atmos. Environ.,* **30,** 563–568.

Schmidlin, F. J., 1988: WMO international radiosonde comparison phase II final report, instruments and observing methods. Rep. 29, WMO/TD-No. 312, World Meteorological Organization, 113 pp.

Smith, W. L., 1970: Iterative solution of the radiative transfer equation for the temperature and absorbing gas profile of an atmosphere. *Appl. Opt.,* **9,** 1993–1999.

——, and Coauthors, 1990: GAPEX: A ground-based atmospheric profiling experiment. *Bull. Amer. Meteor. Soc.,* **71,** 310–318.

——, X. L. Ma, S. A. Ackerman, H. E. Revercomb, and R. A. Knuteson, 1993: Remote sensing of cloud properties from high resolution infrared observations. *J. Atmos. Sci.,* **50,** 1708–1720.

——, W. F. Feltz, R. O. Knuteson, H. E. Revercomb, H. M. Woolf, and H. B. Howell, 1999: The retrieval of planetary boundary layer structure using ground-based infrared spectral radiance measurements. *J. Atmos. Oceanic Technol.,* **16,** 323–333.

Solheim, F., J. R. Godwin, E. R. Westwater, Y. Han, S. J. Keihm, K. Marsh, and R. Ware, 1998: Radiometric profiling of temperature, water vapor and cloud liquid water using various inversion methods. *Radio Sci.,* **33,** 393–404.

Spänkuch, D., W. Döhler, J. Güldner, and A. Keens, 1996: Ground-based passive atmospheric remote sounding by FTIR emission spectroscopy—First resuls with EISAR. *Contrib. Atmos. Phys.*, **69,** 97–111.

——, ——, ——, and E. Schulz, 1998: Estimation of the amount of tropospheric ozone in a cloudy sky by ground-based Fourier-transform infrared emission spectroscopy. *Appl. Opt.,* **37,** 3133–3142.

——, ——, and ——, 1999: Spectral measurements of the the greenhouse effect of biogenous aerosol by ground-based FTIR emission spectroscopy. Preprints, *10th Conf. on Atmospheric Radiation,* Madison, WI, Amer. Meteor. Soc., 556–559.

——, ——, and ——, 2000: Effect of coarse biogenic aerosol on downwelling infrared flux at the surface. *J. Geophys. Res.*, **105** (D13), 17 341–17 350.

Stankov, B. B., 1998: Multisensor retrieval of atmospheric properties. *Bull. Amer. Meteor. Soc.*, **79,** 1835–1854.

Stokes, G. M., and S. E. Schwartz, 1994: The Atmospheric Radiation Measurement (ARM) program: Programmatic background and design of the Cloud and Radiation Testbed. *Bull. Amer. Meteor. Soc.*, **75,** 1201–1221.

Thompson, O. E., 1982: HIRS-ATMS satellite sounding system test—Theoretical and empirical vertical resolving power. *J. Appl. Meteor.,* **21,** 1550–1561.

Troitsky, A.V., K. P. Gaikovich, V. D. Gromov, E. N. Kadygrov, and A. S. Kosov, 1993: Thermal sounding of the atmospheric boundary layer in the oxygen band center at 60 GHz. *IEEE Trans. Geosci. Remote Sens.,* **31,** 116–120.

Ware, R., and Coauthors, 2000: SuomiNet: A real-time national GPS network for atmospheric research and education. *Bull. Amer. Meteor. Soc.,* **81,** 677–694.

Westwater, E. R., 1997: Remote sensing of tropospheric temperature and water vapor by integrated observing systems. *Bull. Amer. Meteor. Soc.,* **78,** 1991–2006.

——, and Coauthors, 1999a: Ground-based remote sensor observations during PROBE in the tropical western Pacific. *Bull. Amer. Meteor. Soc.,* **80,** 257–270.

——, Y. Han, V. G. Irisov, V. Leuskiy, E. N. Kadygrov, and S. A. Viazankin, 1999b: Remote sensing of boundary layer temperature profiles by a scanning 5-mm microwave radiometer and RASS: Comparison experiments. *J. Atmos. Oceanic Technol.,* **16,** 805–818.

——, ——, and F. Solheim, 2000: Resolution and accuracy of a multifrequency scanning radiometer for temperature profiling. *Microwave Radiometry and Remote Sensing of Earth's Surface and Atmosphere,* P. Pamploni and S. Paloscia, Eds., VSP Press, 129–135.

Wilczak, J. M., E. E. Gossard, W. D. Neff, and W. L. Eberhard, 1996: Ground-based remote sensing of the atmospheric boundary layer: 25 years of progress. *Bound.-Layer Meteor.,* **78,** 321–349.